An experimental and numerical study of the mechanical response of 3D printed PLA/CB polymers

Robin Delbart, Aris Papasavvas, Colin Robert, Thuy Quynh Truong Hoang, Francisca Martinez-Hergueta

Composite Structures 319 (2023) 117156

Contents lists available at ScienceDirect

Composite Structures

journal homepage: www.elsevier.com/locate/compstruct

An experimental and numerical study of the mechanical response of 3D printed PLA/CB polymers

Robin Delbart [a], Aris Papasavvas [b], Colin Robert [b], Thuy Quynh Truong Hoang [c], Francisca Martinez-Hergueta [a,*]

[a] School of Engineering, Institute for Infrastructure and Environment, University of Edinburgh, UK
[b] School of Engineering, Institute for Materials and Processes, University of Edinburgh, UK
[c] ESTACA, Pôle Mécanique des Structures Composites et Environment, Ecole d'ingénieurs, France

ARTICLE INFO

Dataset link: https://github.com/RobinDelbart

Keywords:
Additive manufacturing
Crystallinity
Mechanical response
Modelling

ABSTRACT

Fused Filament Fabrication is an Additive Manufacturing method that can produce bespoke components due to the high number of printing parameters available. Each of them plays a significant role in the final mechanical properties of the 3D printed device. This study aimed to uncouple the role of the mesostructure and crystallinity in the final mechanical performance of carbon black/PLA 3D printed samples as a function of the printing parameters. A thermodynamic model was developed to determine the influence of printing parameters, such as nozzle diameter and layer height, in the final crystallinity. Specimens were mechanically tested under uniaxial tensile loads to determine the main deformation and failure mechanisms and results showed that samples were strongly influenced by the printing direction. Furthermore, the nozzle diameter played a significant role in the mesostructure and failure mechanisms, resulting in large differences in ductility for samples printed at raster direction 45°. It was also found that the layer height had a strong influence on the temperature profile and the resulting crystallinity. The importance of crystallinity over porosity to improve the ductility of the material is a substantial contribution to the current state of the art. This work provides the basic fundamentals to manufacturing 3D printed components with tailored mechanical properties for specific loading conditions.

1. Introduction

Additive manufacturing (AM) is an affordable process that allows the production of complex shapes with minimal waste compared to the classic subtractive manufacturing processes [1]. The most widespread manufacturing method is Fused Filament Fabrication (FFF), also called Fused Deposition Modelling, where a solid material (usually a raw filament) is pushed through a hot nozzle at a temperature above glass transition temperature but under melting temperature. Subsequently, the quasi-melted filament is deposited on the bed sheet layer by layer building the part from the bottom to the top [2]. This method allows printing with a large range of materials which includes thermoplastic polymers [3], metal matrix composites [4–6], ceramic [7] or natural fibre-reinforced composites [6,8,9].

The mechanical response of FFF semi-crystalline polymer components depends on the degree of crystallinity and the internal mesostructure, composed of a repeatable sequence of filaments and voids. At the same time, both of them are established by the printing parameters. The current literature reports the influence of the printing parameters in the mechanical response as a function of the internal mesostructure, and neglects completely the role of crystallinity. For instance, reported analysis for 3D printed PLA include the influence of the printing angle [10,11], layer thickness [12–14], infill percentage (also called infill density) [15,16] or printing speed [17,18]. Those studies focused on the correlation between void content and mechanical properties, and do not take into consideration the coupled role of the thermal history and the crystallisation rate. Crystallinity has an important impact on material properties such as stiffness and strength, and is also directly linked to those printing parameters. Further efforts to uncouple the role of thermal history and mesostructure are needed to develop a full understanding of the physical phenomena involved during the 3D printing process.

Numerical and analytical models have been employed to provide additional understanding of the physics involved, however, modelling the whole FFF process is a challenging multidisciplinary task that involves the combination of several numerical tools, from Computational Fluid Dynamics to Finite Element Analysis. Currently, there is a lack of holistic simulation frameworks that can cover all the different stages of FFF. In summary, the numerical/analytical studies available focus

* Corresponding author.
E-mail address: francisca.mhergueta@ed.ac.uk (F. Martinez-Hergueta).

https://doi.org/10.1016/j.compstruct.2023.117156
Received 19 January 2023; Received in revised form 19 April 2023; Accepted 15 May 2023
Available online 19 May 2023

on (a) the melting of the filament in the nozzle and the prediction of the deposition temperature [19–22], (b) the flow simulation of the deposited filament [23,24], (c) the welding between filaments [25–28], (d) the thermal exchange between the previously deposited layer and the deposited one [29–31], and (e) the prediction of the degree of crystallinity of semi-crystalline polymers [32]. Due to the complexity of each building block, the models available in the literature combine up to three of the previous physical mechanisms. For instance, several authors have developed models to predict the degree of crystallinity of polymers such as PLA, PAEKs or PEEK [29,30,33], but they considered a constant deposition temperature at the nozzle hot-end, simplifying the outcomes from previous investigations that prove the melting process results in a heterogeneous temperature profile at the hot-end of the nozzle [19]. These differences in deposition temperature can drastically modify the crystallinity of deposited polymers and affect the mechanical properties of 3D printed parts [34]. These simplifications limit the applicability of the numerical modes to specific printing setups, since they cannot fully decouple the role of the mesostructure and the crystallinity for a set of printing parameters. This has a detrimental impact on the overall design exercise of 3D printed components, and hinders the optimisation of the mechanical response for structural applications.

This paper presents an experimental and numerical approach to determine the impact of different printing parameters (printing angle, layer height and nozzle's diameter) in the final mechanical response of 3D printed carbon black particle/PLA as a function of the mesostructure and the degree of crystallinity. Anisotropic mechanical properties in terms of stiffness, strength, and strain to failure are characterised for each set of parameters. Fractographies are employed to shed light into the different failure modes triggered. A numerical model is introduce to determine the role of the thermal history and predict the crystallinity of each configuration. To increase the accuracy of reported approaches, this model estimates the temperature of the filament during the melting process inside the nozzle and simulates the heat transfer process during FFF afterwards. That information is combined with the crystallisation kinetics to obtain the crystallinity degree of each material point. This investigation provides the basic fundamentals to design 3D printed components with tailored mechanical properties for different loading conditions.

2. Material & methods

2.1. Materials and manufacturing

The material selected for this study is a commercial Polylactic Acid (PLA) filament with the brand name Proto-Pasta supplied by the company Protoplant. The filament is based on the Natureworks 4043 PLA polymer reinforced with carbon black (CB) particles. This material was selected due to its suitability for multifunctional structural applications. The PLA/CB filament is a multifunctional Shape Memory Polymer that offers: (i) high stiffness at room temperature, (ii) a glass transition temperature within an operational range for aerospace applications and (iii) high electrical conductivity. This makes it suitable for a large range of applications, including 4D-printed devices with superior load bearing capacity and additional functionality [35,36].

The specimens were manufactured by a Prusa i3 MK3S FFF printer. A hot-end temperature of 225 °C and a printing bed temperature of 60 °C were used as recommended by the manufacturer, with a fix deposition velocity of 30 mm/s. Two different nozzle diameters were chosen (0.4 and 1 mm) at 100% extrusion ratio. Furthermore, different layer heights of 0.05, 0.1 and 0.2 mm were selected. Moreover, three different printing angles were studied, following two protocols, ASTM D638 for the printing angle ±45° with respect to the loading direction and ASTM D3039 for the 0° and 90° according to Fig. 1. One perimeter layer was included. All specimens had the same thickness of 3.2 mm. This testing matrix included the parameters with a higher impact on the mechanical performance, and provided sufficient experimental results to validate the theoretical model described in Section 3. Furthermore, this set of printing parameters avoided the generation of bubble-like effects [37]. Additionally, the samples were tabbed using epoxy glass boards according to the ASTM D3039. The porosity was characterised using an Archimedes density kit and a Denvwe SI-234 scale.

2.2. Mechanical characterisation

The quasi-static tensile characterisation was performed using an MTS Criterion 45 Series 4 screw-driven frame following the ASTM D6387 standard under stroke control at a cross head speed of 2 mm/min. Additionally, a 2D video extensometer was used to acquire the local longitudinal and transverse strains. The polymer specimens (black due to their carbon filler), were speckled with white paint to enable contrast and capture the local strain field using an Imetrum camera at 5 fps and 1392 × 1038 pixels resolution. The analysis was performed with the software VIC 2D provided by Correlated Solutions. Window size and distance were selected to provide at least 2600 tracking points per image. 5 specimens were tested per configuration (layer height, printing angle and nozzle diameter). The force and strain data were processed with a Python script to obtain the Young's modulus, the ultimate strength, and the elongation at break of every sample.

Post-mortem specimens were inspected using a TM4000Plus Scanning Electron Microscope (SEM) manufactured by Hitachi (Tokyo, Japan) with a 15 kV accelerating voltage and a working distance of 50 mm. The fractographies of the cracked surfaces were taken to identify the failure modes of each configuration and see the welded filament before failure, see Fig. 2.

2.3. Thermal characterisation

The particle content was determined by Thermal Gravimetric Analysis (TGA). TGA was conducted in a nitrogen atmosphere using a Mettler Toledo TGA/DSC 1 at a heating rate of 10 °C/min in the temperature range 30 to 600 °C. TGA curves and derivatograms were recorded to obtain the loss of weight with the evolution of the temperature.

The thermal properties were investigated by Differential Scanning Calorimetry (DSC). The characterisation was carried out in a nitrogen atmosphere using a PerkinElmer DSC 8000. Prior to testing, each specimen was weighted and placed in an aluminium pan, sealed with an aluminium cover. The specimen temperature was stabilised at 30 °C for 5 min and then heated up to 220 °C (above the melting temperature) at a constant rate of 10 °C/min. This analysis provided the thermogram curves (heat flow as a function of temperature) to identify the glass transition temperature, the cold crystallisation temperature and the melting temperature. The degree of crystallinity was calculated according to eq (1) [38]:

$$X_c = \frac{1}{w}\frac{\Delta H_m - \Delta H_c}{\Delta H_m^0}, \tag{1}$$

where ΔH_m and ΔH_c are the enthalpies of fusion and cold recrystallisation of the specimen respectively and ΔH_m^0 is the enthalpy of fusion for 100% crystalline PLA, taken from the literature as 93 J/g [39]. w stands for the PLA mass fraction obtained from the TGA and normalises the result considering the percentage of carbon black particles in the material [40].

Moreover, the crystallisation speed has been investigated within the cold recrystallisation range. Samples extracted from the raw PLA filament were heated above the melting temperature at 220 °C and held for 5 min in order to delete the thermal history. Subsequently, the samples were rapidly cooled in one minute at a fixed temperature T (80 °C, 90 °C, 110 °C and 120 °C) to ensure they kept a fully amorphous structure. Afterwards, the temperature T was held for 30 min to determine the evolution of crystallinity over time.

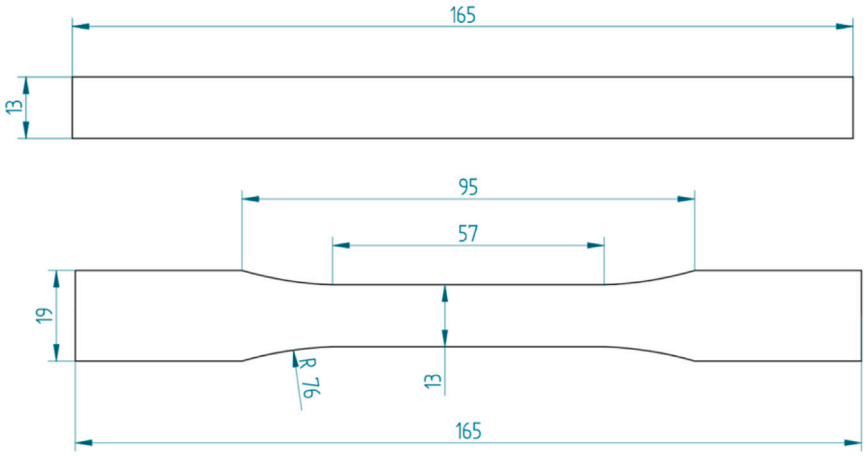

Fig. 1. Dimensions of the coupons used for the mechanical characterisation (both samples have the same thickness of 3.2 mm). (a) Samples for the 0° and 90° printing angles (according to ASTM D3039) and (b) ±45° printing angle (according to ASTM D6387).

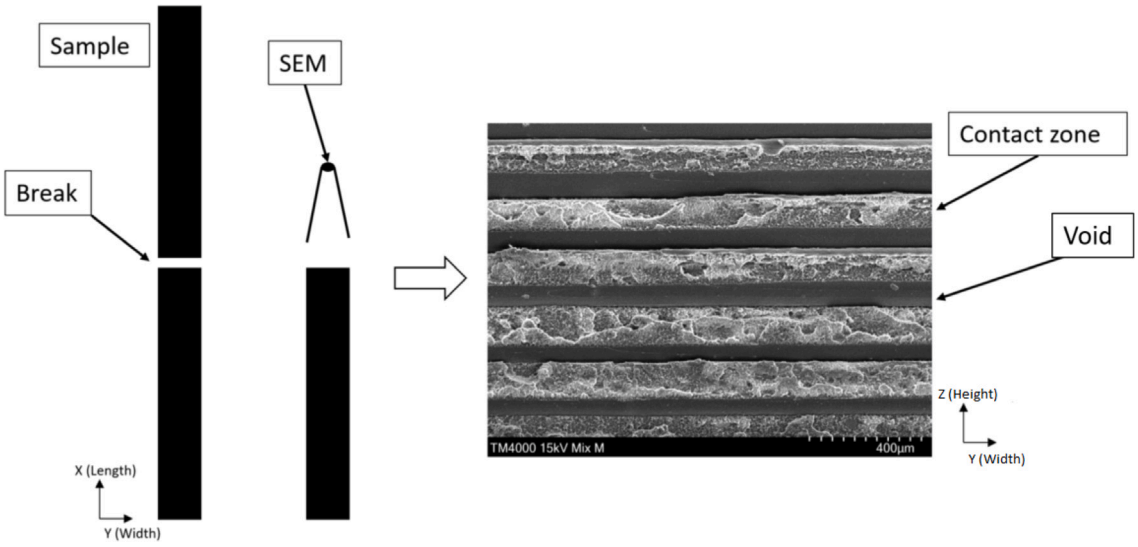

Fig. 2. Procedure to conduct the SEM fractography measurements after tensile testing on the crack surface..

The crystallisation speed $V_{X_c}(T(t))$ as a composite function of the held temperature and time was determined according to:

$$V_{X_c}(T(t)) = \omega \frac{\partial X_c(T(t))}{\partial t}, \tag{2}$$

where $X_c(T(t))$ is the relative crystallinity, calculated according to the method suggested by Su et al. [41] defined as:

$$X_c(T(t)) = \frac{\int_t^{t+dt} H(T(t))\,dt}{\int_0^{t_F} H(T(t))\,dt}, \tag{3}$$

where $H(T(t))$ stands for the enthalpies and t_F is the final time.

3. Modelling

This section summarises the theoretical framework to predict the crystallinity degree of each sample as a function of their unique thermal history defined by the printing temperature, the geometry of the nozzle, the printing speed and the layer height. This model aims to predict the temperature of the filament since it is melted in the nozzle, during deposition and until it reaches thermal equilibrium at the temperature of the printing bed.

3.1. Theoretical model

A theoretical model is proposed to determine the thermal history of the manufactured components and compute the crystallinity degree. It provides: (i) the deposition temperature of the filament as a function of the nozzle diameter (ii) the thermal interaction between the extruded filament (hot) and those previously deposited and (iii) the time evolution of the crystallinity degree for each material point. It should be emphasised that the purpose of these analyses is not to reproduce with high fidelity all the thermodynamic interactions during the printing process, but rather to determine the physics involved and identify the role of each parameter.

First, the melting of the filament in the nozzle is reproduced. The main boundary conditions assume the entering filament is at room temperature (e.g. 20 °C), the material in contact with the walls of the nozzle is at the pre-selected printing temperature (e.g. 225 °C), and the material at the centre of the nozzle is at its coldest temperature, as suggested in [19]. The heat transfer is assumed radially through conduction, i.e. the filament is heated from its external surface to its centre and no heat transfer along the Z axis of a nozzle is considered. Therefore, on each section of the nozzle, the thermal exchange is described by the partial differential equation (PDE):

$$\frac{\partial^2 T(r,t)}{\partial r^2} + \frac{1}{r}\frac{\partial T(r,t)}{\partial r} = \frac{1}{a}\frac{\partial T(r,t)}{\partial t}, \tag{4}$$

where $T(r,t)$ is the temperature in [K] of the filament at the distance r in [m] from its centre and at the time t in [s], and a is the thermal diffusion coefficient of the filament in [m^2/s], constant along the length of the nozzle and independent on the solid or fluid state of the polymer.

If the movement of the melted filament is considered laminar and friction between the polymer and the walls of the nozzle is negligible, all points on a horizontal section of the filament move at the same speed towards the exit of the nozzle. This assumption implies that one can link the time t and the location z of a given section of the filament in the nozzle with the following equation:

$$z = t\frac{F}{\pi R(z)^2}, \tag{5}$$

where $R(z)$ is the radius [m] of the nozzle with respect to the location z, and F is the volume flow rate [m^3/s].

Then, by combining Eqs. (4) and (5) with the initial boundary conditions, the temperature of the filament, T, with respect to its location in the nozzle, (r,z), can be obtained. The temperature of the filament at the end of the nozzle is used afterwards as input for the interlayer heat transfer model. If the thermal exchange with the atmosphere due to convection is neglected, and the heat transfer is assumed to be performed vertically through the layers due to conduction, it can be modelled by the following PDE:

$$\frac{\partial^2 T(z,t)}{\partial z^2} = \frac{1}{a}\frac{\partial T(z,t)}{\partial t}, \tag{6}$$

where this time $T(z,t)$ is the temperature in [K] at the level z in [m] of the printed material point at time t in [s]. If the printing velocity is slow enough to ensure thermal equilibrium has been reached in the previously deposited layers, the main boundary condition is imposed by the temperature of the warm printing plate, i.e. previous layers are initially at a constant temperature of $T_\infty = 60$ °C. The transient heat transfer as a function of the filament geometry can be introduced through the Newton's law of cooling [42,43]:

$$\frac{T(z,t)-T_\infty}{T(z,0)-T_\infty} = e^{-bt} \tag{7}$$

where b represents the cooling rate:

$$b = \frac{h_T A}{\rho V C_p} \tag{8}$$

where h_T is the heat transfer coefficient, A is the heat transfer surface area, V is the volume of the filament, C_p is the specific heat capacity and ρ the density. Finally, the evolution of the temperature over time of each material point, $T(z,t)$, can be combined with the crystallisation speed curves obtained experimentally by DSC to calculate the crystallisation degree of the 3D printed polymer according to the expression:

$$X_C(z) = \int_0^{t_F} V_{X_c}(T(z,t))\,dt \tag{9}$$

3.2. Implementation

The previous model has been implemented in the software Python. The complete source code is available for download on GitHub[1]. All the simulations have been run over 4 s, except the worst case scenario (1 mm nozzle and 0.2 mm layer height) that has been run for a longer period of time (10 s) to ensure thermal equilibrium is reached to prove the assumptions of the model are reasonable. The PDEs have been solved using the *pdepe* function solved with the ode15s solver with a relative error tolerance of 10^{-5} [44,45] in combination with the boundary conditions aforementioned and the following geometrical dimensions and material properties.

The value of the thermal diffusion coefficient, $a = 0.105 \cdot 10^{-6}$ m^2/s in Eqs. (4) and (6) has been taken from the literature [46] considering the carbon black particles have a negligible influence in thermal diffusion [47]. The initial volume flow rate, F in Eq. (5), depends on the nozzle diameter and the layer height and the values are summarised in Table 1. The nozzle has been divided in 3 sections with different diameters as illustrated in Fig. 3. The intermediate section has been idealised by a cylindrical section where the diameter is the mean of the top and bottom diameters. Dimensions are provided in Table 2.

[1] https://github.com/RobinDelbart

Table 1
Value of the initial volume flow rate as a function of the layer height and the nozzle diameter.

F (mm^3/s)	Layer height (mm)		
Nozzle diameter (mm)	0.2	0.1	0.05
0.4	3.95	1.97	0.98
1.0	10.41	5.20	2.60

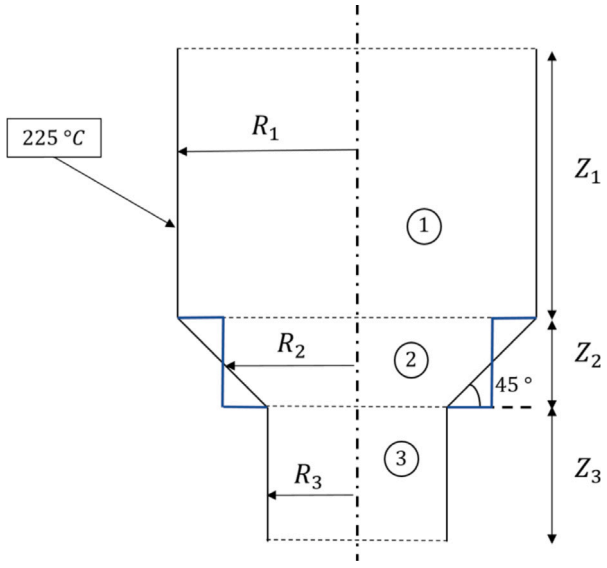

Fig. 3. Nozzle dimensions used for the analytical model.

A slower cooling rate was implemented in the interlayer welding model for the smallest nozzle diameter (0.4 mm) according to:

$$\frac{T_{0.4\ mm}(z,t)-T_\infty}{T_{0.4\ mm}(z,0)-T_\infty} = \frac{T_{1\ mm}(z,t)-T_\infty}{T_{1\ mm}(z,0)-T_\infty}e^{bt} \tag{10}$$

with

$$b = \frac{h_T}{\rho C_p}\left(\frac{A_{1\ mm}}{V_{1\ mm}} - \frac{A_{0.4\ mm}}{V_{0.4\ mm}}\right) \tag{11}$$

where $A_{1\ mm}$, $V_{1\ mm}$, $A_{0.4\ mm}$&$V_{0.4\ mm}$ stand for the area and the volume for the 1 mm nozzle and 0.4 mm nozzle respectively measured by SEM, resulting in a final coefficient $b = 0.0517\ s^{-1}$.

To calculate the crystallinity as defined in Eq. (9), the continuous temperature function $T(z,t)$ obtained from the thermal model has been transformed into a discontinuous step function $T_m(z,t)$ where the mean temperature of the filament at the end of the nozzle has been rounded to the nearest crystallisation speed curve experimentally characterised by DSC. The integral of the composite function over time has been solved numerically using a trapezoidal rule.

4. Results and discussion

4.1. Morphological characterisation

The 3D printed parts present a characteristic periodic mesostructure defined by the filaments, the layers, their respective interfaces (inter- and intra-layer) and voids, see Fig. 4(a). The term filament stands

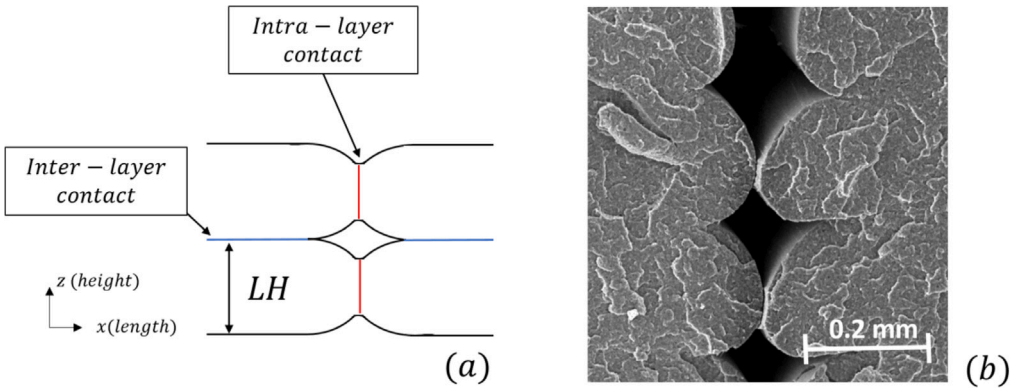

Fig. 4. Morphology of the 3D printed component. (a) Schematic view of two layers of thickness *LH* (layer height) and two adjacent filaments, their intra-layer (highlighted in red) and inter-layer (highlighted in blue) interfaces. (b) SEM micrograph showing the welding differences for each interface. A lack of welding in the intra-layer interface is observed.

Table 2
Numerical value of the nozzle dimensions.

Cylinder	Nozzle	0.4 mm	1 mm
1	R_1 [mm]	0.875	0.875
	Z_1 [mm]	3.825	4.125
2	R_2 [mm]	0.5375	0.6875
	Z_2 [mm]	0.675	0.375
3	R_3 [mm]	0.2	0.5
	Z_3 [mm]	1.5	1.5

for the strands of polymer extruded and deposited, meantime the term layer refers to the horizontal section composed of several filaments. The layer height (LH) of the filament is equivalent to the thickness of each layer. The intra-layer contact (highlighted in red in Fig. 4) refers to the interfaces between adjacent filaments within a layer, and the inter-layer contact (highlighted in blue in Fig. 4) stands for the interface between layers. Voids are systematically located between the interfaces parallel to the printing direction. As the nozzle deposits the melted polymer, it reheats and welds the filaments, consolidating the interfaces. The SEM micrographies show a total melting of the inter-layer interface, but only a partial melting of the intra-layer contact, eventually presenting no consolidation between adjacent filaments for low layer heights, see Fig. 4(b).

Fig. 5 shows the void content of the specimens as a function of the layer height, printing direction and the nozzle diameter characterised using an Archimedes density kit and a scale. When printed with the 1 mm nozzle, large differences are appreciated as a function of the printing angle, with significantly lower porosity when printed along the 0° direction. The porosity decreased with the layer height, however, negligible differences were found for the samples printed at 90°. The smaller nozzle exhibits an overall lower porosity. At lower diameters, the polymer undergoes more compaction, due to the shear stress gradient between the nozzle and the bed, resulting in lower porosity. It can be seen that the layer height also has an influence on porosity for all 0 degrees samples, with the lowest layer height leading to lower porosity. This behaviour can also be explained by the difference in magnitude of the shear stress gradient between the nozzle and the bed, which is more severe when using a lower layer height. However, the effect of layer height on porosity is less significant than the effect of the nozzle diameter.

4.2. Mechanical properties

The mechanical response of the 3D printed carbon reinforced PLA material was characterised as function of the layer height, printing direction and nozzle diameter. The average values of the Young's Modulus, ultimate tensile strength (UTS) and elongation at break are shown in Table 3.

Fig. 6 compares the stiffness of all the configurations against the theoretical value provided by the manufacturer (2.639 GPa). The largest nozzle diameter (1 mm) provides a consistent stiffness regardless of the printing angle and the layer height, close to the manufacturer's value. The difference between the highest average (layer height of 1 mm printed at 45°) and the lowest (layer height of 0.2 mm printed at 0°) is only 0.3 GPa. Nevertheless, the smallest nozzle diameter (0.4 mm) provides a heterogeneous result, with higher stiffness for the 0° printing angle. Previous studies reported increased carbon black reagglomeration for certain manufacturing conditions such as increased temperatures [48–50]. The differences between both nozzle diameters will be further studied by means of thermal and crystallinity analysis in Section 4.4. Overall, for the smallest nozzle diameter, similar stiffness is found for the samples printed at the raster direction 0°, and a significant increment in stiffness with the layer height is observed instead for the samples printed at the raster direction 90°. The deformation mechanisms of the samples and their impact on their mechanical properties will be further analysed in Section 4.3.

Fig. 7 displays the average UTS and the standard deviation. Similar trends are observed for both nozzle diameters, nevertheless, the layer height influences the UTS differently according to the printing angle. At 0° and 45°, the ultimate strength increases when decreasing the layer height. In contrast, the opposite trend is observed with the samples printed at 90°. Overall, a superior strength is obtained for the specimens printed at 0°, replicated by the samples printed at 45° only when manufactured with the biggest nozzle diameter (1 mm).

Fig. 8 shows the elongation at break. Similar trends are found for both nozzle diameters, comparable to the trends of the ultimate strength. The samples printed at 90° present a modest increment of ultimate strain when increasing the layer height, and the opposite trend is appreciated for samples printed at 0°, with a remarkable increment of the ductility in the case of 0.05 mm layer height. The highest elongation at break is registered for the 45° specimens when printed with the smallest nozzle (0.4 mm) and a layer height of 0.1 mm.

4.3. Failure analysis and fractography

The response of the samples printed at 0° is consistent for both nozzle diameters, see Fig. 9, despite the lower porosity of the samples printed with the smallest nozzle diameter (0.4 mm), see Fig. 5. Analysing the results of both nozzle diameters individually, it is observed the mechanical properties decrease with increasing the layer height and the porosity, as expected when testing porous materials. The differences between the mechanical responses for different nozzle diameters will be further analysed by means of crystallinity analysis in Section 4.4. Filament tensile failure is the intrinsic failure mode of this

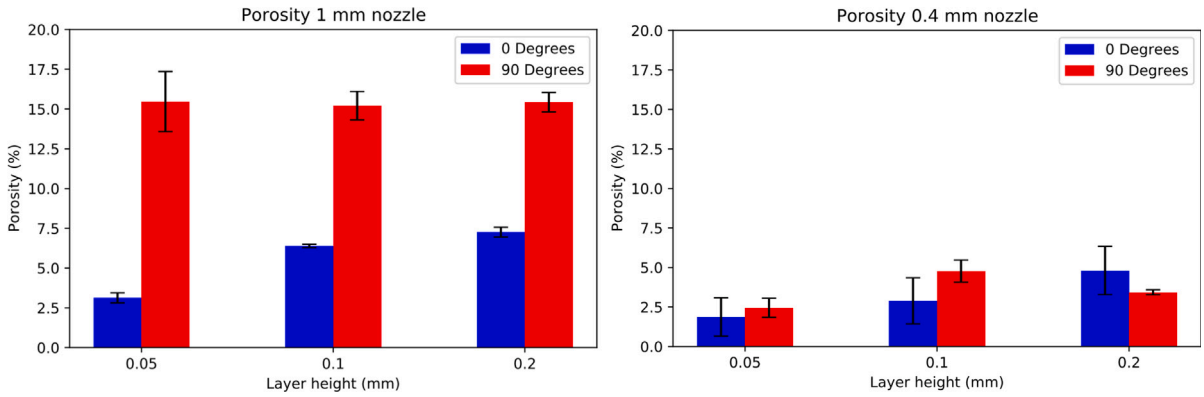

Fig. 5. Porosity (%) as a function of the printing direction and the layer height. (a) 1 mm nozzle diameter and (b) 0.4 mm nozzle diameter.

Table 3
In-plane tensile mechanical properties of the Protopasta filament as function of the printing angle, the nozzle diameter and the layer height.

		Printing angle					
		0°		45°		90°	
		Nozzle diameter					
		1 mm	0.4 mm	1 mm	0.4 mm	1 mm	0.4 mm
Ultimate strength (MPa)	0.2 mm	30.02	29.61	30.35	19.68	17.07	11.89
	0.1 mm	32.21	30.29	31.50	21.07	16.29	7.34
	0.05 mm	36.56	34.38	36.23	29.54	9.38	3.46
Elongation at break	0.2 mm	0.0229	0.0204	0.0231	0.0307	0.0092	0.0071
	0.1 mm	0.0216	0.0236	0.0236	0.0391	0.0084	0.0061
	0.05 mm	0.0369	0.0373	0.0265	0.0337	0.0072	0.0053
Young's modulus (GPa)	0.2 mm	2.301	2.474	2.468	1.593	2.433	2.07
	0.1 mm	2.600	2.543	2.682	1.437	2.494	1.869
	0.05 mm	2.490	2.274	2.543	1.973	1.170	2.433

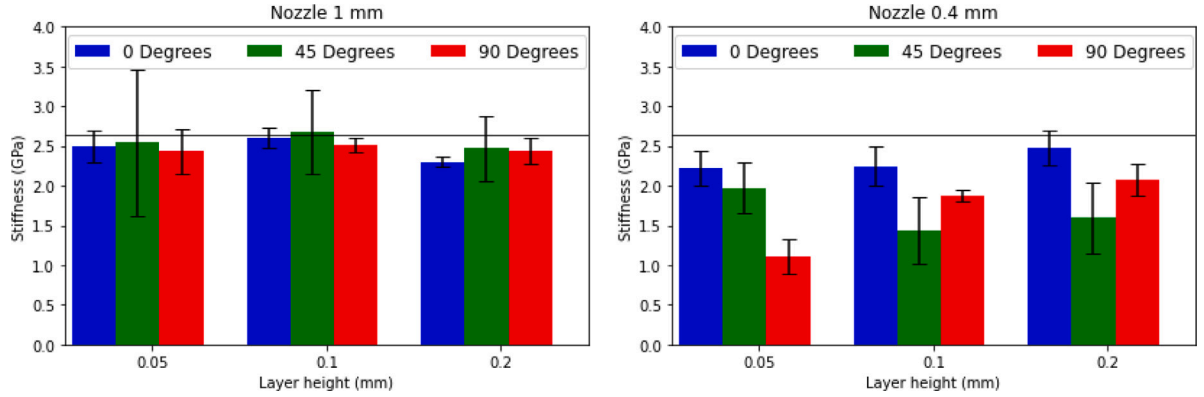

Fig. 6. Young's modulus (GPa) as a function of the printing direction and the layer height. (a) 1 mm nozzle diameter and (b) 0.4 mm nozzle diameter.

printing direction, although depending on the layer height it results in a brittle or a ductile fracture. Fig. 10 compares the brittle fracture surface of the 0.2 mm layer height specimen, and the ductile fracture surface of the thinnest layer height, 0.05 mm. The difference in ductility cannot be justified by the 3D printed mesostructure and, therefore, subsequent crystallinity analysis will be conducted in Section 4.4.

The specimens printed at 90° present a poor mechanical response. The stiffness, strength and strain to failure are directly proportional to the thickness of the layer height and the best performance is found when printing with the biggest nozzle diameter of 1 mm despite the higher porosity, see Fig. 11.

The fracture surfaces have been inspected by SEM and the fractography analysis shows all the specimens fail due to intra-layer debonding, resulting in a brittle failure mode. The intra-layer is the weakest interface of the 3D printed component due to the systematic location of the voids and the eventual lack of welding between adjacent filaments, see Fig. 4, in agreement with previous findings [27]. Figs. 12 and 13 analyse the fracture surfaces (highlighted in red colour) for the biggest nozzle diameter (1 mm) and the different layer heights (0.2 and 0.05 mm respectively). The mechanical properties are directly proportional to the extension of the fractured area, which increases with the layer height and nozzle diameter. In the case of the thickest layer height (0.2 mm, see Fig. 12), weldlines are consistently formed at each layer, resulting in the best mechanical performance. Nevertheless, for thinner layer heights, the experimental width of printing is lower than the theoretical value, hence weldlines are not formed on each layer. As a result, large voids appear in the intra-layer and samples exhibit premature failure, with particularly poor mechanical properties in the case of the thinnest layer height, 0.05 mm, see Fig. 13.

The samples printed at 45° present a different response depending on the nozzle size. Fig. 14 shows the representative stress vs strain curves. The specimens printed with the biggest nozzle (1 mm diameter)

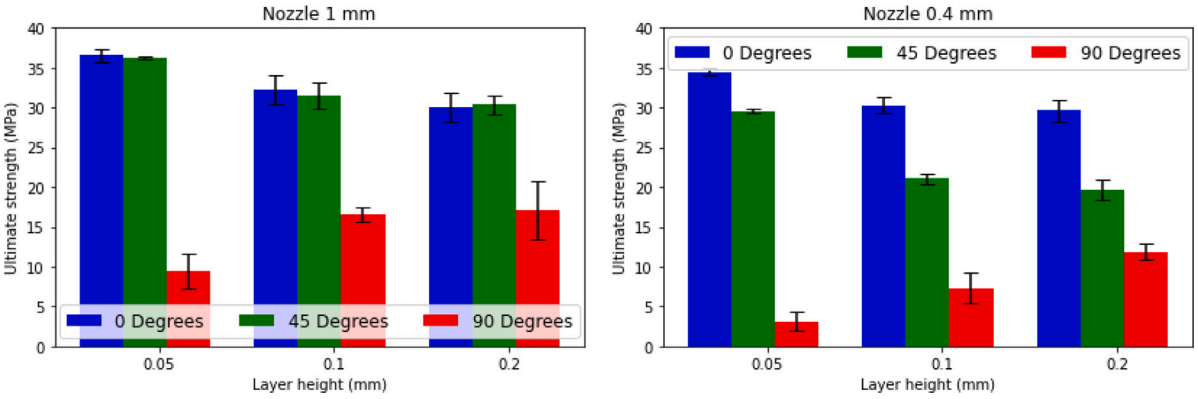

Fig. 7. Ultimate tensile stress (MPa) as a function of the printing direction and the layer height. (a) 1 mm nozzle diameter and (b) 0.4 mm nozzle diameter.

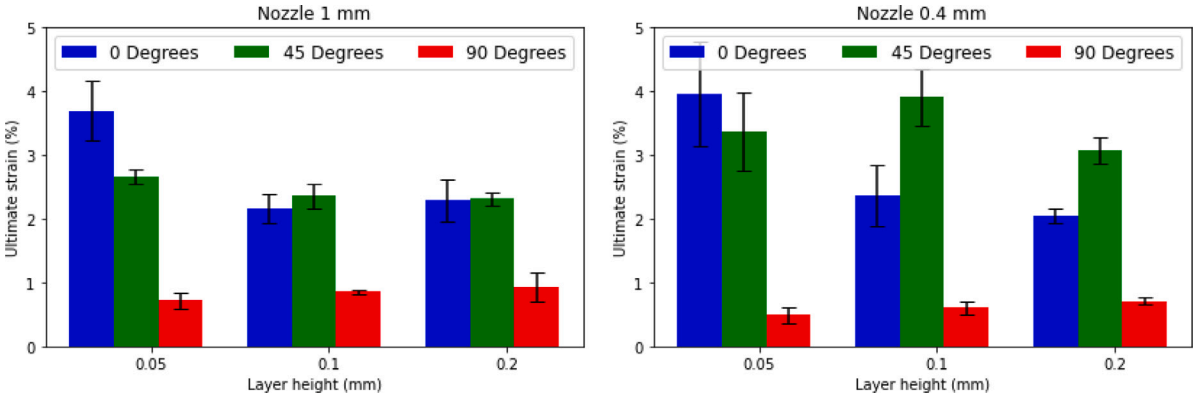

Fig. 8. Ultimate strain (%) as a function of the printing direction and the layer height. (a) 1 mm nozzle diameter and (b) 0.4 mm nozzle diameter.

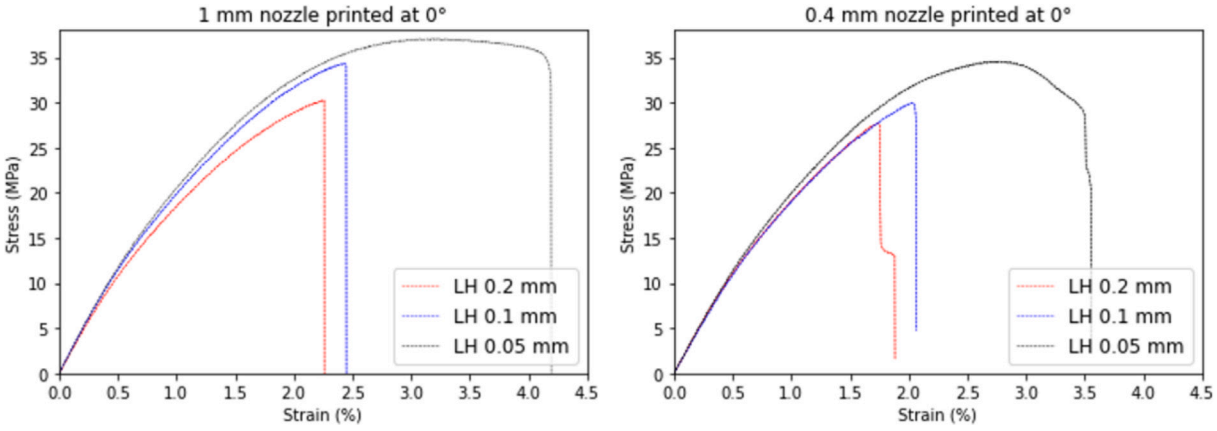

Fig. 9. Representative stress–strain curves for the samples printed at 0° with different nozzle diameters: (a) 1 mm and (b) 0.4 mm.

present a brittle fracture surface. As per samples printed at 0°, the thinner layer heights result in lower porosity and higher mechanical properties (stiffness, strength and strain to failure). In comparison, the specimens printed with the smallest nozzle (0.4 mm diameter) show an elasto-plastic response with a higher elastic compliance. The highest stiffness and strength are registered for the thinnest layer height of 0.05 mm.

The differences in mechanical response are a result of the deformation and failure mechanisms triggered during the loading process for each configuration. In the case of the specimens printed with the biggest nozzle diameter (1 mm), the behaviour is driven by two main failure mechanisms: (i) intra-layer debonding and (ii) filament brittle tensile failure. A homogeneous strain distribution is exhibited until 2% of deformation when intra-layer debonding is triggered, see Fig. 15.

As the elongation progresses, the tensile strength of PLA is overtaken resulting in the final failure of the specimen. Fig. 16 shows the SEM fractography and the crack path, formed by a succession of filament debonding and tensile rupture. The relatively large width of the filaments (1.2 mm) promotes through-thickness crack propagation, minimising the fracture surface.

In the case of the specimens printed with the smallest nozzle diameter (0.4 mm), there is one additional failure mechanism to consider: through-thickness inter-layer debonding. The large compliance appreciated in the stress–strain curves, see Fig. 14(b), is a result of the higher number of interfaces and the lower welding capacity of these printing

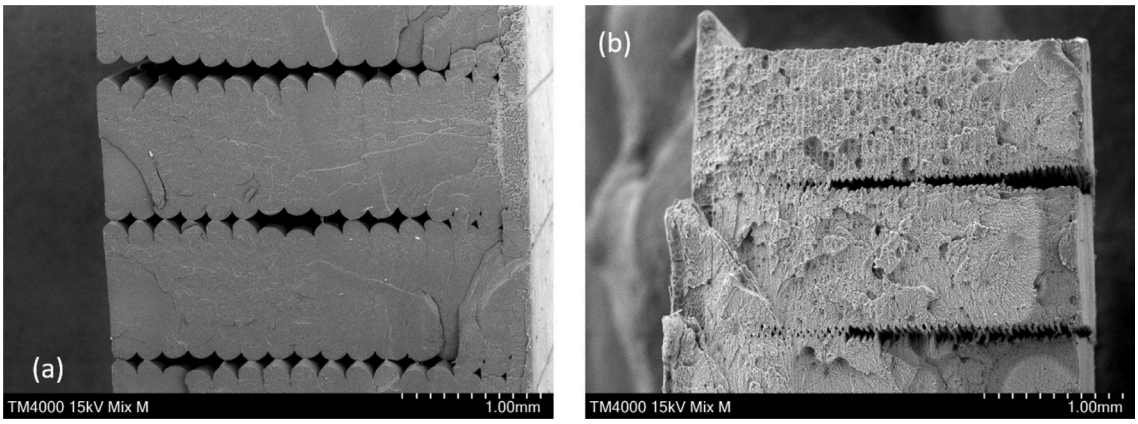

Fig. 10. Fractographies of samples printed at 0° and (a) 0.2 mm and (b) 0.05 mm layer heights respectively.

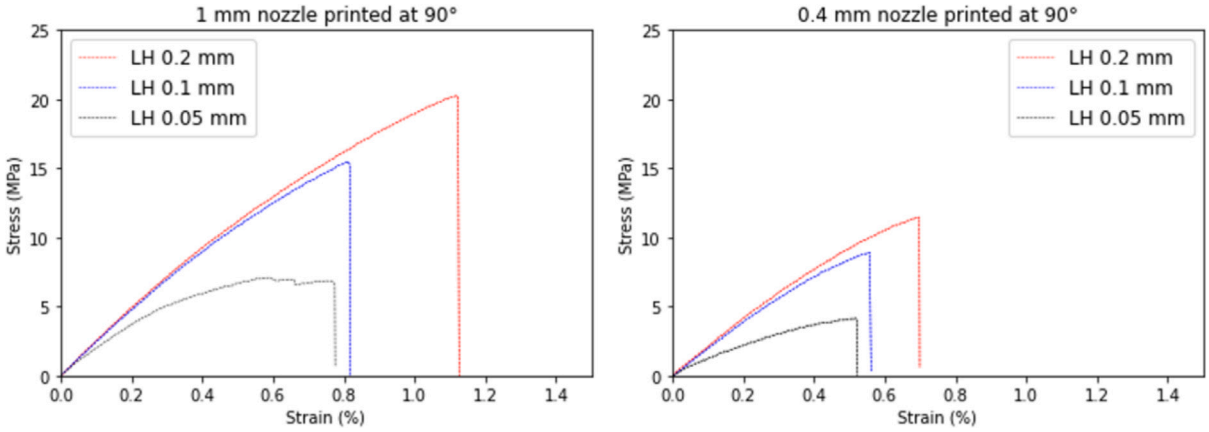

Fig. 11. Representative stress–strain curves for samples printed at 90° with different nozzle diameters: (a) 1 mm and (b) 0.4 mm.

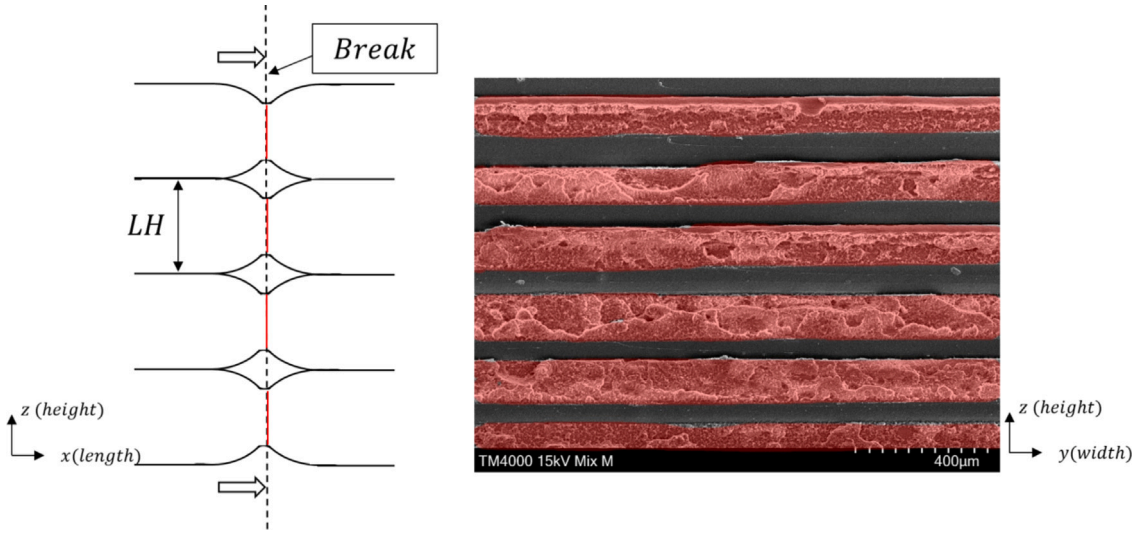

Fig. 12. Fractography for the samples printed at 90° with a layer height of 0.2 mm and 1 mm nozzle diameter.

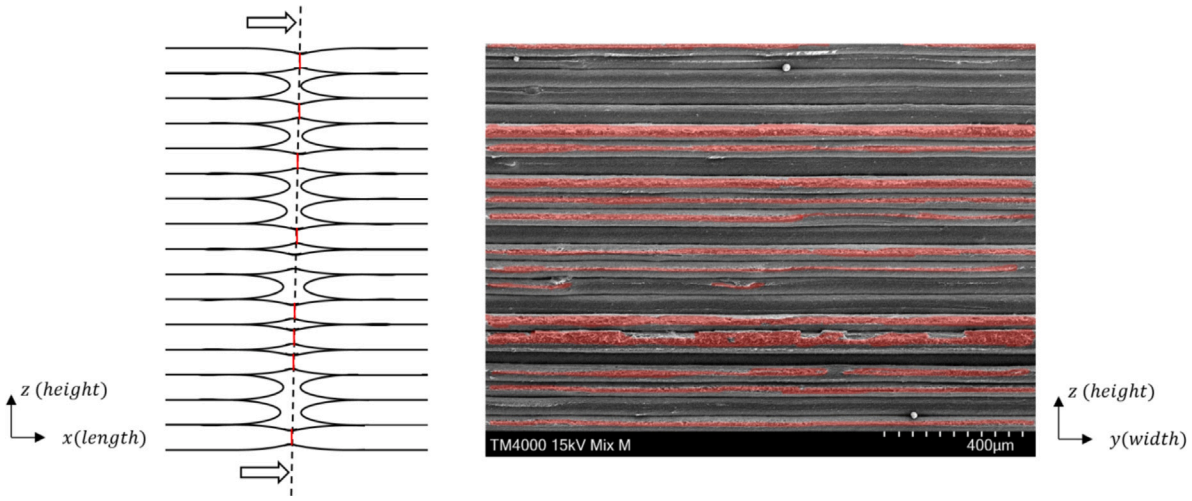

Fig. 13. Fractography for the samples printed at 90° with a layer height of 0.05 mm and 1 mm nozzle diameter.

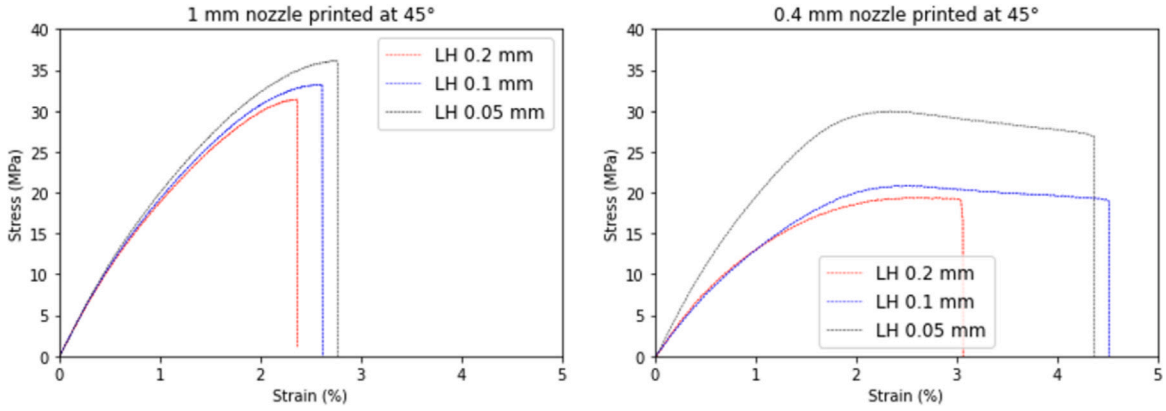

Fig. 14. Representative stress–strain curves for the samples printed at 45° with different nozzle diameters: (a) 1 mm and (b) 0.4 mm.

parameters. Fig. 17 shows the DIC full-field of the strain along the loading axis. The first failure mechanisms, intra-layer and inter-layer debonding, are triggered at 2.18% of deformation. As a result, detached filaments tend to rotate and align towards the loading direction without increasing the external force applied. The final failure of the specimen happens due to filament brittle tensile failure. A longer crack path is generated for this configuration as a result of the interlayer debonding, see Fig. 18.

4.4. Thermal properties, history and crystallinity

Fig. 19 shows the DSC thermograms of the 3D printed samples and the as-received raw filament. Three characteristic temperatures can be distinguished: (i) the transition temperature, T_g (57.54 °C and 60.89 °C for the samples printed with the 1 mm nozzle and the 0.4 mm nozzle respectively regardless of the layer height), (ii) the cold crystallisation exotherm peak, T_c (103.33 °C and 105.86 °C for the 1 mm and 0.4 mm nozzles respectively) and (iii) the melting peak, T_m (153.65 °C and 154.57 °C for the 1 mm and 0.4 mm nozzles respectively). The crystallisation rate has been calculated considering a weight percentage of PLA $w = 0.56$ determined by TGA. Table 4 resumes all the crystallisation rates as a function of the layer height and nozzle diameter.

The peak temperatures are quite homogeneous for all the layer heights. The cold recrystallisation and melting temperatures are in agreement with the conventional values reported for PLA, within the 100–130 °C and 120–180 °C ranges respectively [51]. The as-received raw filament presents a fully amorphous structure characteristic of PLA

Table 4
Degree of crystallinity for 1 mm and 0.4 mm nozzle diameter samples at different layer heights at raster direction 0°.

Layer height (mm)	0.05	0.1	0.2	Raw filament
X_c 1mm nozzle (%)	2.80	10.32	15.78	0.21
X_c 0.4 mm nozzle (%)	1.48	5.41	13.31	

samples cold down homogeneously [52]. The heating cycles imposed by the 3D printing process increase the degree of crystallinity of the PLA, up to a maximum of ≈ 15%, however, the 0.05 mm layer height configuration still results in a fully amorphous polymer. These values are in agreement with previous findings which report that overall crystallisation rates of PLA in homogeneous conditions are relatively low [51]. When printed with the smallest nozzle the crystallisation is globally lower with a bigger difference between the 0.2 mm layer height and the 0.1 mm layer height. The degree of crystallinity correlates with the ductility of the filaments. The higher percentage of amorphous chains in the specimens with a 0.05 mm layer height justify the increment of ultimate strain as reported in Fig. 8 and explain why the mechanical properties of 0.4 mm are lower, despite the lower porosity, see Fig. 5. These findings demonstrate the importance of crystallinity over porosity to improve the mechanical properties of 3D printed structures.

Fig. 20 plots the isothermal DSC curves at different temperatures. Fig. 20(a) illustrates the change of the heat flow, Fig. 20(b) shows the relative crystallinity according to Eq. (3) and Fig. 20 (c) plots the

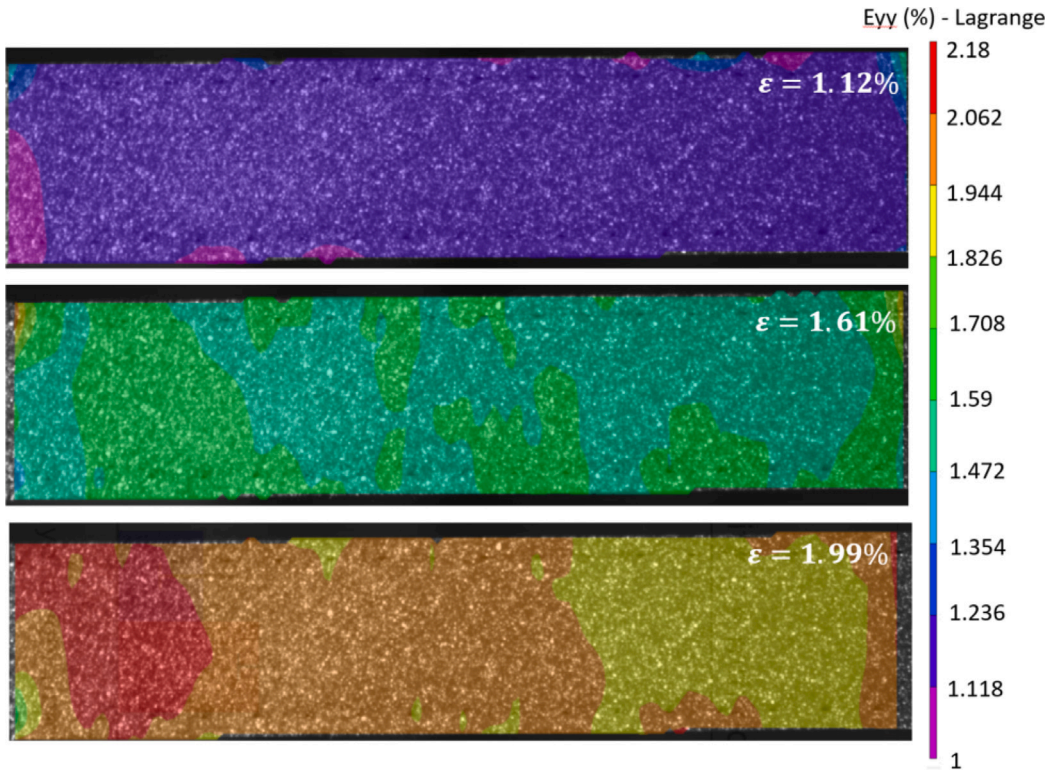

Fig. 15. Contour plots of the evolution of engineering strain in the loading direction at different applied strains for the specimens printed at 45° with the 1 mm nozzle diameter & 0.1 mm layer height. (a) 1.12% deformation, (b) 1.61% deformation and (c) 1.99% deformation.

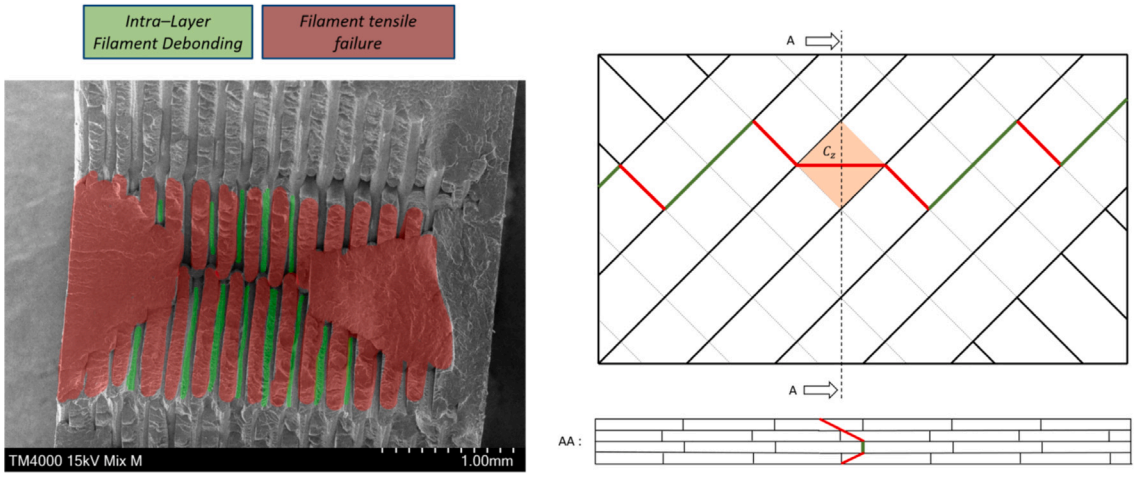

Fig. 16. Failure analysis of the specimens printed at 45° with the 1 mm nozzle diameter & 0.1 mm layer height. (a) SEM fractography. (b) Frontal and (c) side schematics views of the crack path.

crystallisation speed obtained from equation (2). Lower temperatures (e.g. 80 and 90 °C) require additional time to activate the crystallisation process, but result in a higher crystallisation degree and speed afterwards in comparison to higher temperatures, in agreement with the findings by Balazs et al. [53].

The degree of crystallinity of the 3D printed samples depends on the thermal history of each specimen, defined by the analytical model described in Section 3. The left hand side of Fig. 21 provides the warming process of the centre of the filament while crossing the nozzle for the three layer heights, and the right hand side of Fig. 21 shows the estimated temperature profile of the filaments while exiting the nozzle for each configuration. The lowest temperature in the centre of the filament is predicted for the largest layer height, 0.2 mm, and the biggest nozzle diameter, 1 mm. The temperature gradient on the extruded filament varies for each layer height as a result of the different volume flow rates to ensure a constant printing speed for all the configurations. Hence, the largest layer height (0.2 mm) requires the fastest volume flow rate, so the processing time (the period of time that takes the filament to cross through the nozzle) is not sufficiently long to warm up the centre of the filament, which barely reaches 140 °C for the biggest nozzle size. In the same way, the smallest layer height (0.05 mm) requires a volume flow rate slow enough to heat the filament homogeneously for both nozzle diameters, with a negligible drop in temperature in the centre of the filament, from the original 225 °C to 224 °C for the biggest nozzle size. The nozzle diameter also has an impact on the temperature gradient achieved in the filament. The heat transfer is more efficient for smaller nozzle sizes as the processing time is longer and the volume of material is lower. As a result, the

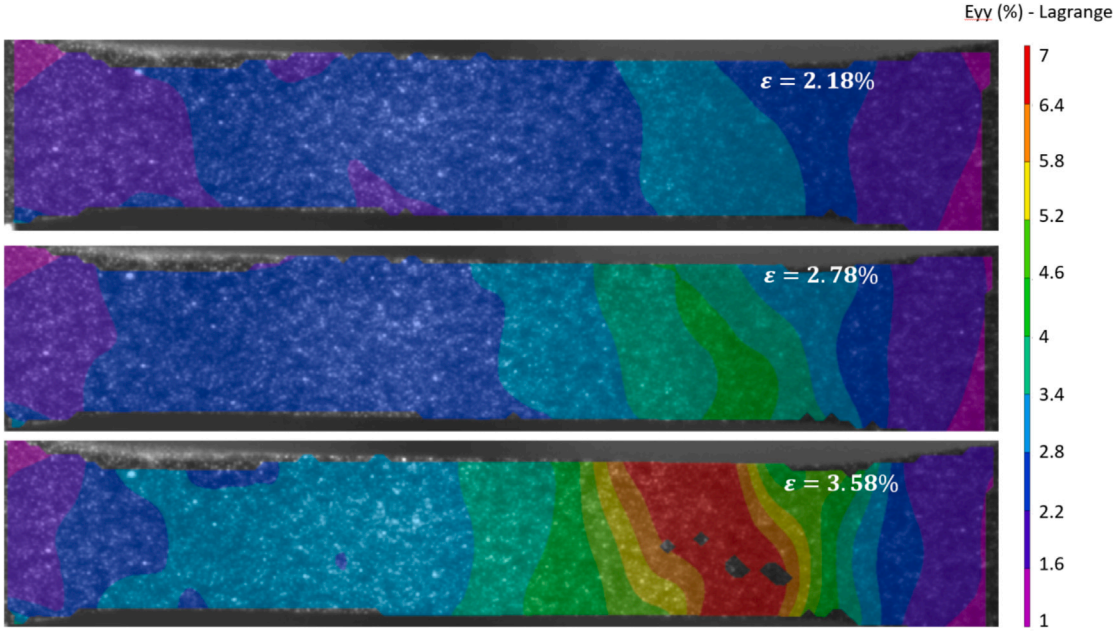

Fig. 17. Contour plots of the evolution of engineering strain in the loading direction at different applied strains for the specimens printed at 45° with the 0.4 mm nozzle diameter & 0.1 mm layer height. (a) 2.18%deformation, (b) 2.78% deformation and (c) 3.58% deformation.

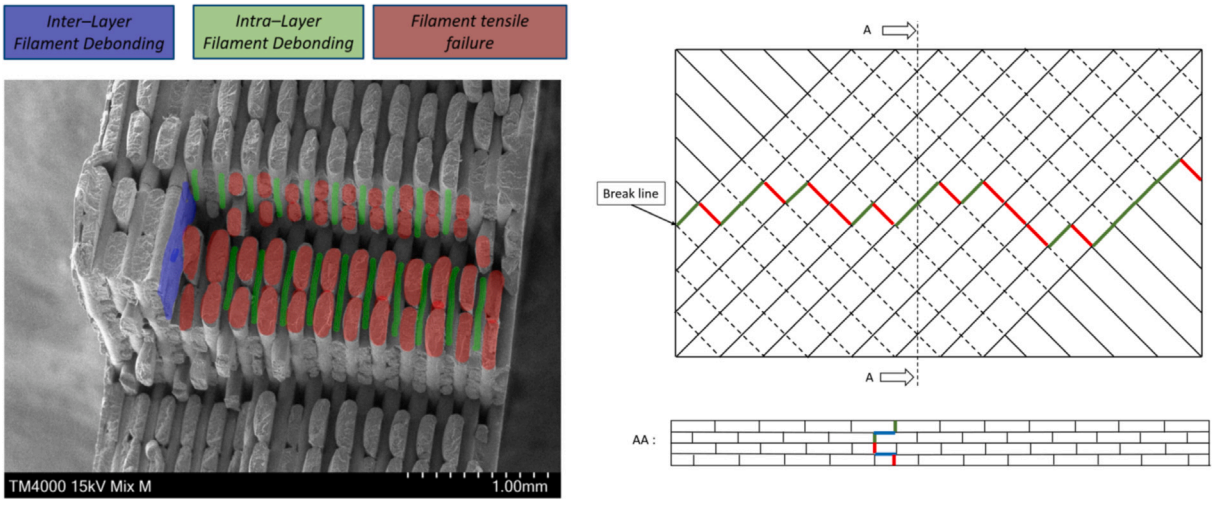

Fig. 18. Failure analysis of the specimens printed at 45° with the 0.4 mm nozzle diameter & 0.1 mm layer height. (a) SEM fractography. (b) Frontal and (c) side schematics views of the crack path.

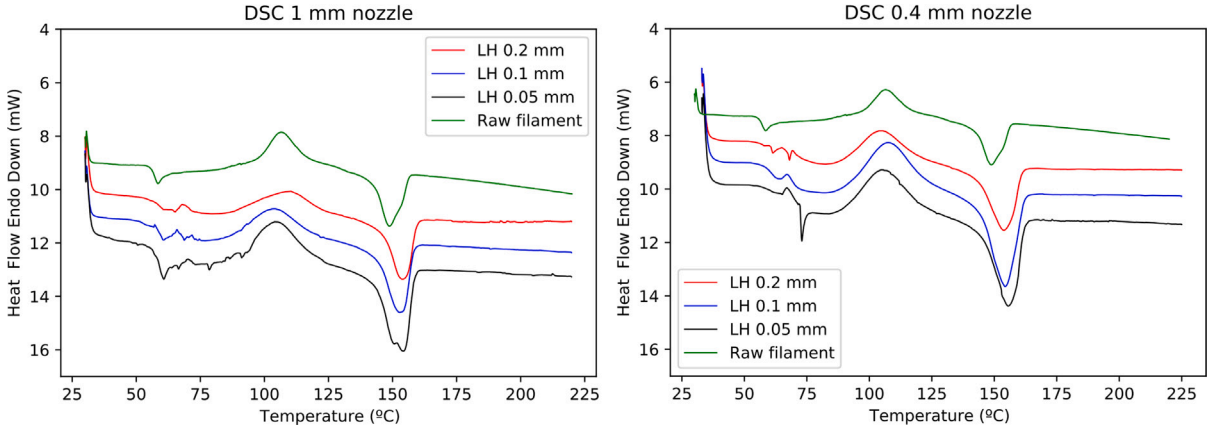

Fig. 19. DSC curves for samples printed with the (a) 1 mm nozzle and (b) 0.4 mm nozzle.

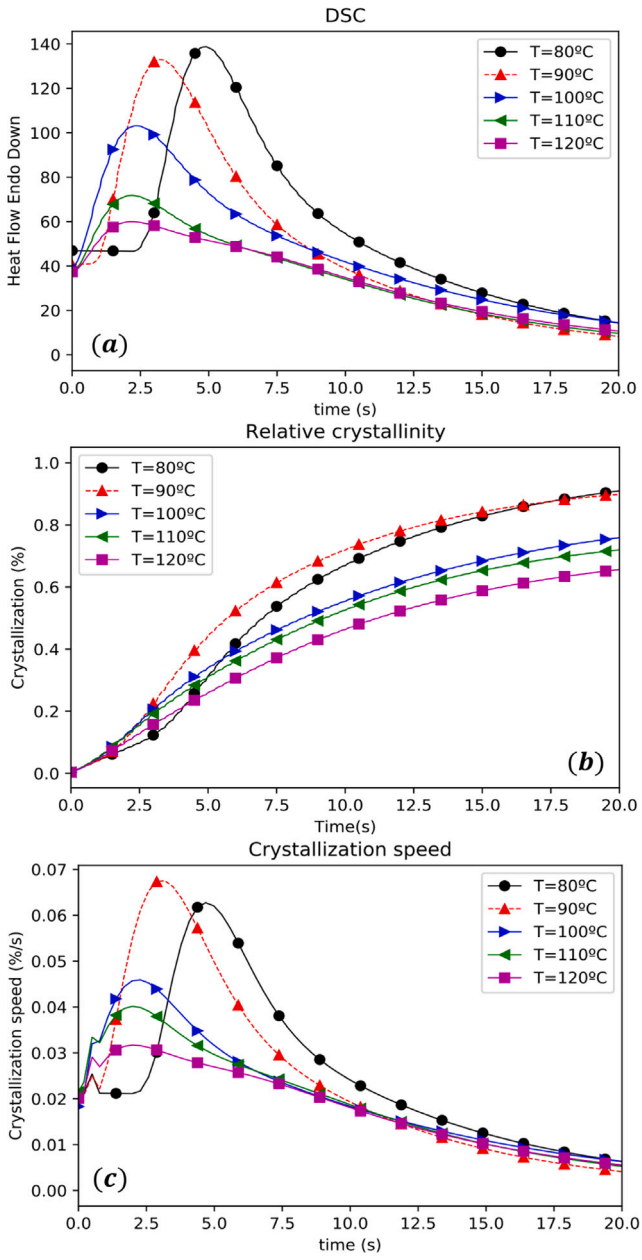

Fig. 20. Isothermal DSC curves. (a) Heat flow, (b) relative crystallisation and (c) crystallisation speed.

0.4 mm nozzle achieves relatively homogeneous filament temperatures meanwhile large gradients are appreciated for the highest nozzle size and large layer height.

The mean temperature at the end of the nozzle, T_m, is used as input of the interlayer heat transfer model to analyse the thermal history of the 3D printed specimens. Fig. 22 compares the temperature distribution and cooling time for all the configurations once a new filament (at level 0 mm in height) is deposited over the previous layers measured in the centre axis of the nozzle. As the hot filament contacts the previous layer it induces a superficial melt, welding both layers together. The thermal inertia determines the thermal history of the previously deposited layers, therefore, the thicker the layer height and the higher the deposition temperature, the higher the temperature achieved by the adjacent layers. The thinnest layer height (0.05 mm) offers a limited capacity to reheat the previous layers above the cold recrystallisation temperature. Fig. 22 shows that temperatures higher than 100 °C are only achieved at a maximum depth of 0.05 mm, and for a period of time lower than 0.2 s. On the other hand, the configuration with the highest thermal inertia (0.2 mm layer height and 0.4 mm nozzle diameter) is able to increase the temperature of the previous layers well beyond the cold crystallisation temperature up to 0.15 mm depth for a period of time longer than 1 s. These results are in agreement with the study presented by Xia et al. [31], who found that the volume of material involved in the heat exchange process was proportional to the thermal inertia.

To predict the degree of crystallinity of the 3D printed component, the thermal history was combined with the crystallisation speeds according to Eq. (9). The heating cycles were replicated simulating the deposition of a reference filament and 4 additional layers on top every four seconds. Fig. 23 illustrates the time evolution of the average temperature and crystallinity of the reference filament for 0.05 mm and 0.2 mm layer heights respectively, printed with the 1 mm diameter nozzle. The two horizontal lines represent the cold crystallisation regime. As defined in the theoretical model, crystallinity only increases if the cold crystallisation temperature is reached, and it is directly proportional to the period of time within that region. Thinner layer heights (e.g. 0.05 mm) impose high input temperatures but very fast cooling rates. As a result, cold crystallisation is activated 3 times (the deposition of the reference filament plus two additional layers on top), but its capacity to increase is limited, resulting in an amorphous polymer, see Fig. 23(a). On the other hand, thicker layer heights (e.g. 0.2 mm) exhibit large increments of crystallinity due to the higher thermal inertia and the slower cooling rates, despite the reduced number of crystallisation cycles, see Fig. 23(b). The same trends are observed for the samples printed with the 0.4 mm nozzle.

Fig. 24 compares the predicted and experimental degrees of crystallinity as a function of the layer height and nozzle diameter. The model captures the main trend; an increment of crystallinity with the layer height. It also captures the lower crystallinity degree exhibited by the samples printed with the 0.4 mm nozzle as a result of the fastest cooling rate of that set of printing parameters. The discrepancies between the experimental results and analytical predictions are a result of the initial assumptions and limitations of the numerical model. First, the extrusion process has assumed no friction between the nozzle walls and the melted filament. Improved accuracy of the temperature profile at the end of the nozzle and a more precise prediction of crystallinity can be obtained when incorporating that mechanism. Second, the conductive thermal exchange between adjacent filaments on the same layer has not been included. The implementation of that mechanism might improve the accuracy for configurations with consolidated intra-layer interfaces (e.g, 1 mm nozzle diameter and high layer heights). Finally, incorporating the natural convection thermal exchange with the environment might be relevant to simulate the printing process of large components with long manufacturing timelines, since local temperature might drop down to room temperature. Despite the limitations, the numerical approach can be extended to analyse the processing of different semicrystalline thermoplastic polymers, including PEEK or Nylon, and additional manufacturing processes such as compression moulding and resin infiltration.

5. Conclusion

The mechanical response of 3D printed components manufactured in carbon black reinforced PLA has been characterised. The influence of different printing parameters (the layer height, the nozzle diameter and the printing direction) has been analysed experimentally. Furthermore, a theoretical model has been developed to study the thermal history, predict the crystallinity of the polymer and understand the influence of each printing parameter in the final mechanical performance. It was found that the mechanical response was driven by the regular filament/void mesostructure and the degree of crystallinity of the 3D

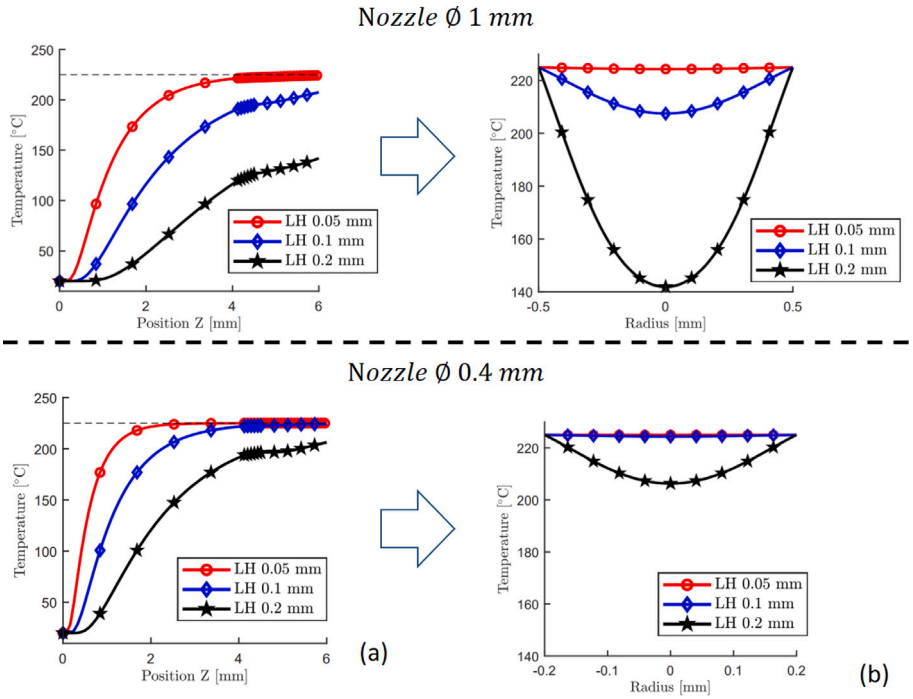

Fig. 21. Predicted filament temperature during processing as a function of the nozzle diameter and the layer height. Left hand side shows the evolution of the temperature at the centre of the filament *vs* the position Z within the nozzle. Right hand side shows the temperature gradient of the filament at $Z = 6$ mm, when exiting the nozzle.

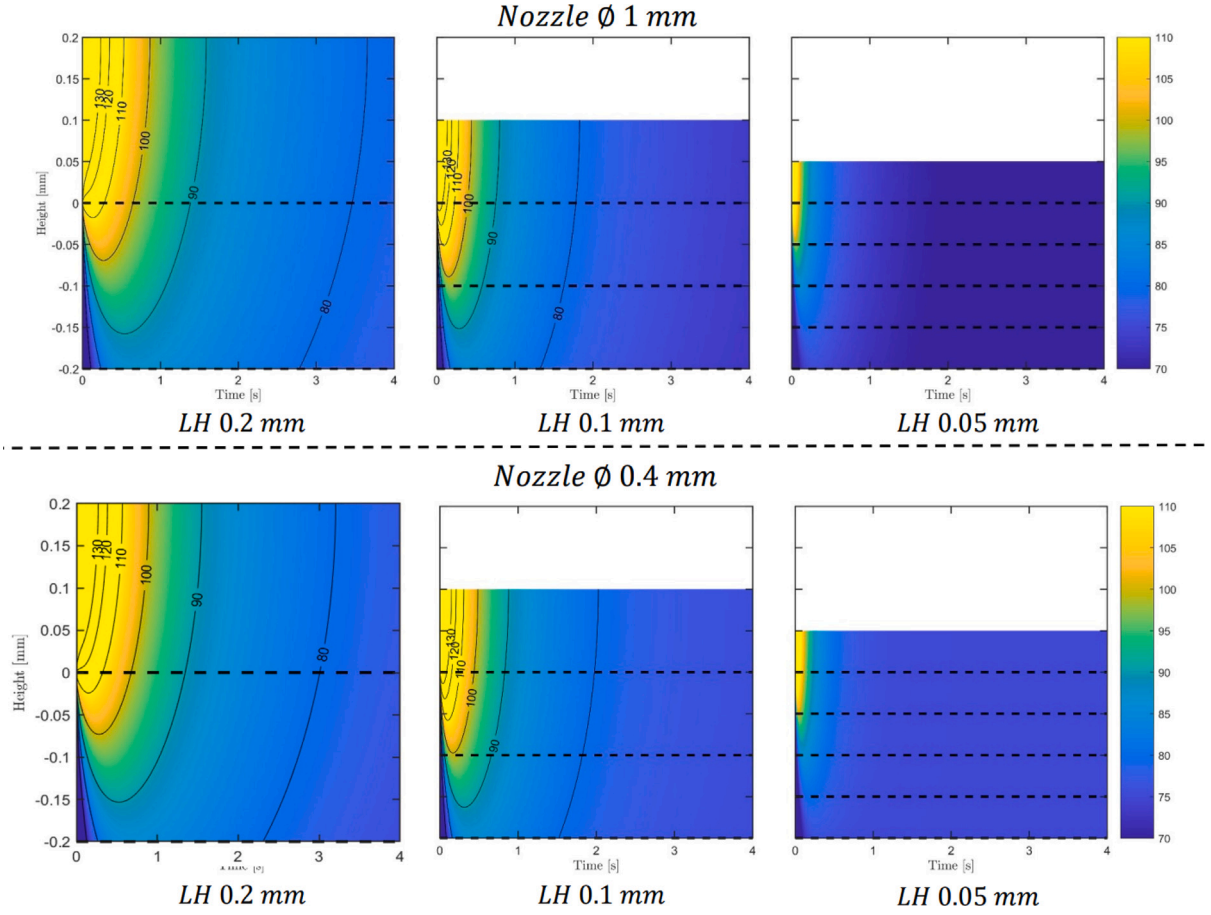

Fig. 22. Time evolution of the temperature distribution through the layers for different layer heights and nozzle diameters.

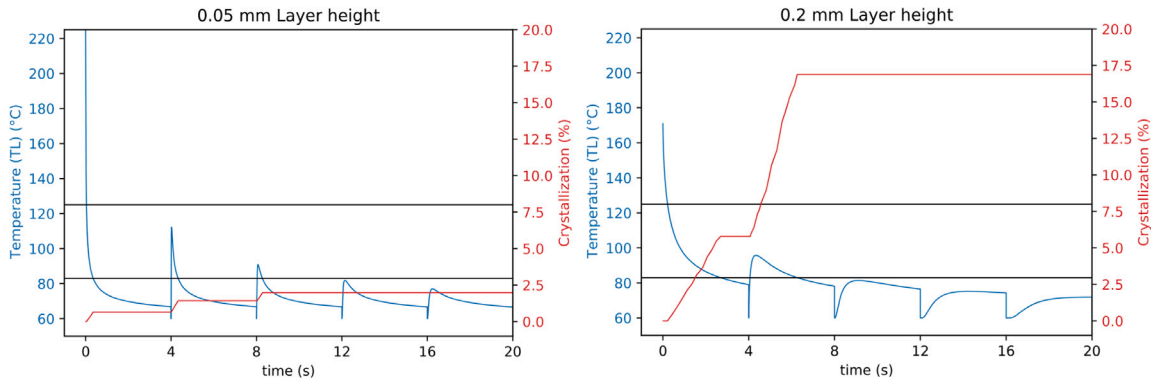

Fig. 23. Time evolution of the temperature and crystallinity of the samples printed with the 1 mm nozzle. (a) 0.05 mm and (b) 0.2 mm layer height. The two horizontal lines represent the cold crystallisation regime.

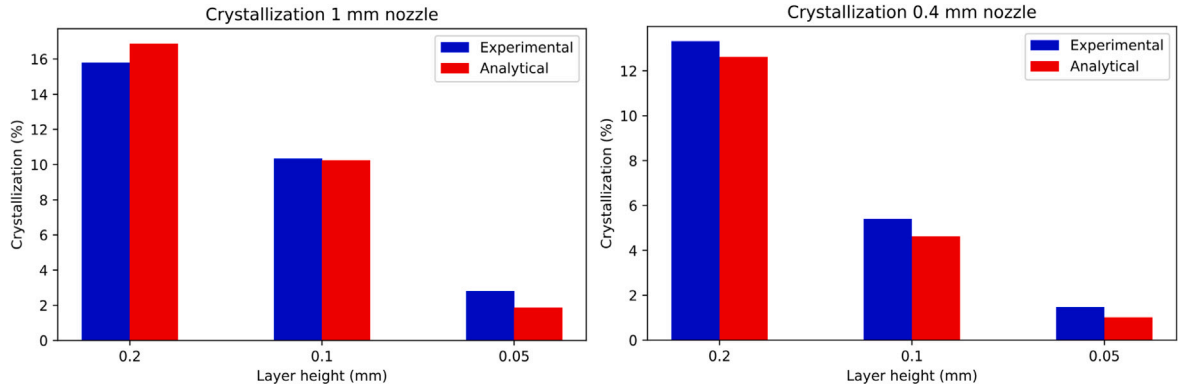

Fig. 24. Experimental vs analytical results of the crystallisation for the (a) 1 mm nozzle diameter and (b) 0.4 mm nozzle diameter.

printed material. As a result, each configuration exhibited different deformation and failure mechanisms.

Best mechanical properties in terms of stiffness and strength were obtained for the configurations printed at 0° direction with the biggest nozzle (1 mm diameter) and the smallest layer height (0.05 mm). These samples exhibited the lowest porosity, showing the relevance of the mesostructure in the mechanical performance. On the other hand, the samples printed at 90° showed very poor mechanical properties as a result of the inefficient welding of the intra-layer interface, eventually showing no contact between filaments for low layer heights.

Damage tolerance of the 3D printed components was dictated by the deformation and failure mechanisms, which differed for each configuration. Samples printed at 90° failed due to intra-layer debonding, resulting in a brittle failure mode. Samples printed at 45° presented different failure mechanisms depending on the number of interfaces. Configurations with a lower number of interfaces (e.g. 1 mm nozzle diameter) exhibited filament brittle tensile failure and intra-layer filament debonding, leading to an overall brittle response. On the other hand, samples with a higher number of interfaces (e.g. 0.4 mm nozzle diameter) presented an additional failure mode; through-thickness inter-layer filament debonding. This additional mechanism promoted filament rotation and realignment towards the loading direction, showing improved damage tolerance. Samples printed at 0° failed due to filament tensile failure and intra-layer filament debonding, however, depending on the layer height, brittle or ductile fashions were found due to differences in crystallinity of the 3D printed polymers.

The theoretical model provided valuable insight into the thermal history of the manufactured components. First, the deposition temperatures for different layer heights and nozzle diameters were analysed. It was found the smallest nozzle (0.4 mm) presented homogeneous heating of the filament. Larger nozzle diameters and flow rates (to print higher layer heights) resulted in heterogeneous temperature gradients of the filament profile at the end of the nozzle. Afterwards, the thermal interaction between deposited filaments was studied. The 3D printing process induced thermal cycles on the previously deposited layers. The heat exchange process was driven by the thermal inertia, as a function of the deposition temperature, the volume and the surface area of the filament. All thermal cycles that induced temperatures above the cold crystallisation temperature promoted the growth of crystalline molecular structures. The configurations with higher thermal inertia (e.g. 0.2 mm layer height) presented a slow cooling rate and a substantial increment of the degree of crystallinity. On the other hand, lower thermal inertia (e.g. 0.05 mm layer height and 0.4 mm nozzle diameter) resulted in a rapid cooling rate and amorphous structures. The higher percentage of amorphous chains led to the ductile failure of the filaments under tension observed in the configurations printed with layer height 0.05 mm and tested along the filament direction. At the same time, the higher degree of crystallinity provided by the biggest nozzle diameter (1 mm) resulted in equivalent stiffness and strength values regardless of the higher porosity in comparison to the response of the samples printed with the 0.4 mm nozzle diameter. These findings highlight the relevance of crystallinity over porosity to improve the mechanical properties of 3D printed semi-crystalline polymers. Furthermore, the numerical approach can be extended to analyse the processing of different semicrystalline thermoplastic polymers, including PEEK or Nylon, and additional manufacturing processes such as compression moulding and resin infiltration.

This investigation provides the necessary engineering fundamentals to design 3D printed components with tailored mechanical properties for different applications. Stiffness and strength can be enhanced by reducing the void content, increasing the crystallinity and aligning the filaments towards the loading direction. Superior ductility can be also reached by minimising the thermal inertia of the deposition process to retain a higher percentage of amorphous molecular chains of the

semicrystalline polymer. Furthermore, improved damage tolerance can be achieved when printing along the ±45° directions with smaller layer heights and nozzle diameters to promote longer crack paths and higher energy dissipation. Printing perpendicularly to the loading direction does not offer any advantage in terms of mechanical performance and should be avoided, and substituted by a non linear infill. These findings will be applied in subsequent publications to design 3D components for low-velocity impact applications.

CRediT authorship contribution statement

Robin Delbart: Investigation, Methodology, Formal analysis, Software, Visualisation, Data curation, Validation, Writing – original draft. **Aris Papasavvas:** Software, Writing – review & editing. **Colin Robert:** Investigation, Methodology, Supervision, Writing – review & editing. **Thuy Quynh Truong Hoang:** Supervision, Conceptualisation, Funding acquisition, Writing – review & editing. **Francisca Martinez-Hergueta:** Supervision, Conceptualisation, Funding acquisition, Formal analysis, Writing – original draft.

Declaration of competing interest

The authors declare that they have no known competing financial interests or personal relationships that could have appeared to influence the work reported in this paper.

Data availability

Data is available in the GitHub link: https://github.com/RobinDelbart.

Acknowledgements

This research is sponsored by the Defense Science and Technology Laboratory (DSTL) (grant number DSTLX1000144021R). The collaboration of Mr. Bence Toth is gratefully acknowledged.

References

[1] Schniederjans Dara G. Adoption of 3D-printing technologies in manufacturing: A survey analysis. Int J Prod Econ 2017;183:287–98.
[2] Cano-Vicent Alba, Tambuwala Murtaza M, Hassan Sk Sarif, Barh Debmalya, Aljabali Alaa AA, Birkett Martin, et al. Fused deposition modelling: Current status, methodology, applications and future prospects. Addit Manuf 2021;47:102378.
[3] Samykano M, Selvamani SK, Kadirgama K, Ngui WK, Kanagaraj G, Sudhakar K. Mechanical property of FDM printed ABS: Influence of printing parameters. Int J Adv Manuf Technol 2019;102(9):2779–96.
[4] Nocheseda Carla Joyce C, Liza Fred P, Collera Alvin Kim M, Caldona Eugene B, Advincula Rigoberto C. 3D printing of metals using biodegradable cellulose hydrogel inks. Addit Manuf 2021;48:102380.
[5] Hwang Seyeon, Reyes Edgar I, Moon Kyoung-sik, Rumpf Raymond C, Kim Nam Soo. Thermo-mechanical characterization of metal/polymer composite filaments and printing parameter study for fused deposition modeling in the 3D printing process. J Electron Mater 2015;44(3):771–7.
[6] Fafenrot Susanna, Grimmelsmann Nils, Wortmann Martin, Ehrmann Andrea. Three-dimensional (3D) printing of polymer-metal hybrid materials by fused deposition modeling. Materials 2017;10(10):1199.
[7] Chen Zhangwei, Li Ziyong, Li Junjie, Liu Chengbo, Lao Changshi, Fu Yuelong, et al. 3D printing of ceramics: A review. J Eur Ceramic Soc 2019;39(4):661–87.
[8] Van de Werken Nekoda, Tekinalp Halil, Khanbolouki Pouria, Ozcan Soydan, Williams Andrew, Tehrani Mehran. Additively manufactured carbon fiber-reinforced composites: State of the art and perspective. Addit Manuf 2020;31:100962.
[9] Blok Lourens G, Longana Marco L, Yu H, Woods Ben KS. An investigation into 3D printing of fibre reinforced thermoplastic composites. Addit Manuf 2018;22:176–86.
[10] Zhang Xinzhou, Chen Lan, Mulholland Tom, Osswald Tim A. Effects of raster angle on the mechanical properties of PLA and Al/PLA composite part produced by fused deposition modeling. Polym Adv Technol 2019;30(8):2122–35.
[11] Algarni Mohammed. The influence of raster angle and moisture content on the mechanical properties of PLA parts produced by fused deposition modeling. Polymers 2021;13(2):237.
[12] Cho Ei Ei, Hein Ho Hin, Lynn Zarni, Hla Saw Jiemie, Tran Thanh. Investigation on influence of infill pattern and layer thickness on mechanical strength of PLA material in 3D printing technology. J Eng Sci Res 2019;3(2):27–37.
[13] Luzanin Ognjan, Movrin Dejan, Stathopoulos Vassilis, Pandis Pavlos, Radusin Tanja, Guduric Vera. Impact of processing parameters on tensile strength, in-process crystallinity and mesostructure in FDM-fabricated PLA specimens. Rapid Prototyp J 2019.
[14] Zhao Yu, Chen Yuansong, Zhou Yongjun. Novel mechanical models of tensile strength and elastic property of FDM AM PLA materials: Experimental and theoretical analyses. Mater Des 2019;181:108089.
[15] Rodríguez-Panes Adrián, Claver Juan, Camacho Ana María. The influence of manufacturing parameters on the mechanical behaviour of PLA and ABS pieces manufactured by FDM: A comparative analysis. Materials 2018;11(8):1333.
[16] Rismalia M, Hidajat SC, Permana IGR, Hadisujoto B, Muslimin M, Triawan F. Infill pattern and density effects on the tensile properties of 3D printed PLA material. 2019;1402(4):044041.
[17] Murugan Ramu, Mitilesh RN, Singamneni Sarat. Influence of process parameters on the mechanical behaviour and processing time of 3D printing. Int J Mod Manuf Technol 2019;1(1):21–7.
[18] Abeykoon Chamil, Sri-Amphorn Pimpisut, Fernando Anura. Optimization of fused deposition modeling parameters for improved pla and ABS 3D printed structures. Int J Lightweight Mater Manuf 2020;3(3):284–97.
[19] Ufodike Chukwuzubelu Okenwa, Nzebuka Gaius Chukwuka. Investigation of thermal evolution and fluid flow in the hot-end of a material extrusion 3D printer using melting model. Addit Manuf 2022;49:102502.
[20] Kattinger Julian, Ebinger Tim, Kurz Raphael, Bonten Christian. Numerical simulation of the complex flow during material extrusion in fused filament fabrication. Addit Manuf 2022;49:102476.
[21] Serdeczny Marcin P, Comminal Raphaël, Mollah Md Tusher, Pedersen David B, Spangenberg Jon. Numerical modeling of the polymer flow through the hot-end in filament-based material extrusion additive manufacturing. Addit Manuf 2020;36:101454.
[22] Bian Yan-Hua, Yu Gang, Zhao Xin, Li Shao-Xia, He Xiu-Li, Tian Chong-Xin, et al. Exit morphology and mechanical property of FDM printed PLA: influence of hot melt extrusion process. Adv Manuf 2022;1–19.
[23] Lei Mingju, Wei Qinghua, Li Mingyang, Zhang Juan, Yang Rongbin, Wang Yanen. Numerical simulation and experimental study the effects of process parameters on filament morphology and mechanical properties of FDM 3D printed PLA/GNPs nanocomposite. Polymers 2022;14(15):3081.
[24] Kim Sun Kyoung, Kazmer David O. Non-isothermal non-Newtonian three-dimensional flow simulation of fused filament fabrication. Addit Manuf 2022;55:102833.
[25] Costa SF, Duarte FM, Covas JA. Estimation of filament temperature and adhesion development in fused deposition techniques. J Mater Process Technol 2017;245:167–79.
[26] Pokluda Ondřej, Bellehumeur Céline T, Vlachopoulos John. Modification of Frenkel's model for sintering. AIChE J 1997;43(12):3253–6.
[27] Garzon-Hernandez S, Garcia-Gonzalez D, Jérusalem A, Arias A. Design of FDM 3D printed polymers: An experimental-modelling methodology for the prediction of mechanical properties. Mater Des 2020;188:108414.
[28] Rando Pietro, Ramaioli Marco. Numerical simulations of sintering coupled with heat transfer and application to 3D printing. Addit Manuf 2022;50:102567.
[29] Schiavone Nicola, Verney Vincent, Askanian Haroutioun. Effect of 3D printing temperature profile on polymer materials behavior. 3D Print Addit Manuf 2020;7(6):311–25.
[30] Brenken Bastian, Barocio Eduardo, Favaloro Anthony, Kunc Vlastimil, Pipes R Byron. Development and validation of extrusion deposition additive manufacturing process simulations. Addit Manuf 2019;25:218–26.
[31] Xia Huanxiong, Lu Jiacai, Dabiri Sadegh, Tryggvason Gretar. Fully resolved numerical simulations of fused deposition modeling. Part I: fluid flow. Rapid Prototyp J 2018.
[32] Ovlaque Pierre, Bayart Marie, Soulestin Jérémie, Trolez Yves, Olivier Dominique, Bujeau Benjamin, et al. On the temperature evolution and related crystallinity of polypropylene parts processed via material extrusion. Addit Manuf 2022;58:103065.
[33] Yi Nan, Davies Richard, Chaplin Adam, McCutchion Paul, Ghita Oana. Slow and fast crystallising poly aryl ether ketones (PAEKs) in 3D printing: Crystallisation kinetics, morphology, and mechanical properties. Addit Manuf 2021;39:101843.
[34] Collinson David W, von Windheim Natalia, Gall Ken, Brinson L Catherine. Direct evidence of interfacial crystallization preventing weld formation during fused filament fabrication of poly (ether ether ketone). Addit Manuf 2022;102604.
[35] Delbart Robin, Martinez-Hergueta Francisca, Roumy Laurane, Tong Zheng, Robert Colin, Truong-Hoang TQuynh. 4D printed active composites. In: Additive manufacturing of polymer-based composite materials. Accepted Manuscript. Elsevier.
[36] Roumy Laurane, Touchard Fabienne, Marchand Damien, Hoang Thuy Quynh Truong, Martinez-Hergueta Francisca. Durability of joule effect of 3D printed carbon black/polylactic acid: electrical cyclic tests and analytical modelling. Int J Fatigue 2023;107677.

[37] Ferreira Rafael Thiago Luiz, Amatte Igor Cardoso, Dutra Thiago Assis, Bürger Daniel. Experimental characterization and micrography of 3D printed PLA and PLA reinforced with short carbon fibers. Composites B 2017;124:88–100.
[38] Mathew Aji P, Oksman Kristiina, Sain Mohini. The effect of morphology and chemical characteristics of cellulose reinforcements on the crystallinity of polylactic acid. J Appl Polym Sci 2006;101(1):300–10.
[39] Harris Angela M, Lee Ellen C. Improving mechanical performance of injection molded PLA by controlling crystallinity. J Appl Polym Sci 2008;107(4):2246–55.
[40] Inácio Erika Martins, Lima Maria Celiana Pinheiro, Souza Diego Holanda Saboya, Sirelli Lys, Dias Marcos Lopes. Crystallization, thermal and mechanical behavior of oligosebacate plasticized poly (lactic acid) films. PolíMeros 2018;28:381–8.
[41] Su Zhizhong, Guo Weihong, Liu Yongjun, Li Qiuying, Wu Chifei. Non-isothermal crystallization kinetics of poly (lactic acid)/modified carbon black composite. Polym Bull 2009;62(5):629–42.
[42] Belmonte Manuel, Koller Martin, Moyano Juan José, Seiner Hanus, Miranzo Pilar, Osendi María Isabel, et al. Multifunctional 3D-printed cellular MAX-phase architectures. Adv Mater Technol 2019;4(9):1900375.
[43] Mishra Anand Kumar, Pan Wenyang, Giannelis Emmanuel P, Shepherd Robert F, Wallin Thomas J. Making bioinspired 3D-printed autonomic perspiring hydrogel actuators. Nat Protoc 2021;16(4):2068–87.
[44] Shampine Lawrence F, Reichelt Mark W. The matlab ode suite. SIAM J Sci Comput 1997;18(1):1–22.
[45] Shampine Lawrence F, Reichelt Mark W, Kierzenka Jacek A. Solving index-1 DAEs in MATLAB and simulink. SIAM Rev 1999;41(3):538–52.
[46] Marsh JJ, Turner RP, Carter J, Jenkins MJ. Thermal diffusivity and secondary crystallisation kinetics in poly (lactic acid). Polymer 2019;179:121595.
[47] GÜLTEKİN Nergis Demirel, İsmail USTA. Investigation of thermal and electrical conductivity properties of carbon black coated cotton fabrics. Marmara Fen Bilimleri Dergisi 2015;27:91–4.
[48] Bao Yu, Xu Ling, Pang Huan, Yan Ding-Xiang, Chen Chen, Zhang Wei-Qin, et al. Preparation and properties of carbon black/polymer composites with segregated and double-percolated network structures. J Mater Sci 2013;48:4892–8.
[49] Rieker Thomas P, Misono Shinji, Ehrburger-Dolle Françoise. Small-angle X-ray scattering from carbon blacks: Crossover between the fractal and porod regimes. Langmuir 1999;15(4):914–7.
[50] Rieker Thomas P, Hindermann-Bischoff Manuela, Ehrburger-Dolle Françoise. Small-angle X-ray scattering study of the morphology of carbon black mass fractal aggregates in polymeric composites. Langmuir 2000;16(13):5588–92.
[51] Saeidlou Sajjad, Huneault Michel A, Li Hongbo, Park Chul B. Poly (lactic acid) crystallization. Prog Polym Sci 2012;37(12):1657–77.
[52] Jiménez Alfonso, Peltzer Mercedes, Ruseckaite Roxana. Poly (lactic acid) science and technology: processing, properties, additives and applications. (12). Royal Society of Chemistry; 2014.
[53] Balazs Adam. Crystallization kinetics of commercial PLA filament. Commun Sci Lett Univ Zilina 2017;19(4):15–9.